Coherent laser-millimeter-wave interactions en route to coherent population transfer

Citation: Grimes, David D. et al. "Coherent Laser-Millimeter-Wave Interactions En Route to Coherent Population Transfer." The Journal of Chemical Physics 147, 14 (October 2017): 144201

As Published: http://dx.doi.org/10.1063/1.4997624

Publisher: American Institute of Physics (AIP)

Persistent URL: http://hdl.handle.net/1721.1/115168

Version: Final published version: final published article, as it appeared in a journal, conference proceedings, or other formally published context

Coherent laser-millimeter-wave interactions en route to coherent population transfer

David D. Grimes, Timothy J. Barnum, Yan Zhou, Anthony P. Colombo, and Robert W. Field

Citation: The Journal of Chemical Physics **147**, 144201 (2017); doi: 10.1063/1.4997624
View online: https://doi.org/10.1063/1.4997624
View Table of Contents: http://aip.scitation.org/toc/jcp/147/14
Published by the American Institute of Physics

Coherent laser-millimeter-wave interactions en route to coherent population transfer

David D. Grimes,[1] Timothy J. Barnum,[1] Yan Zhou,[2] Anthony P. Colombo,[1,a)] and Robert W. Field[1,b)]
[1]*Department of Chemistry, Massaschusetts Institute of Technology, Cambridge, Massachusetts 02139, USA*
[2]*JILA, National Institute of Standards and Technology, Department of Physics, University of Colorado, Boulder, Colorado 80309-0440, USA*

(Received 25 July 2017; accepted 11 September 2017; published online 9 October 2017)

We demonstrate coherent two-photon population transfer to Rydberg states of barium atoms using a combination of a pulsed dye laser and a chirped-pulse millimeter-wave spectrometer. Numerical calculations, using a density matrix formalism, reproduce our experimental results and explain the factors responsible for the observed fractional population transferred, optimal experimental conditions, and possibilities for future improvements. The long coherence times associated with the millimeter-wave radiation aid in creating coherence between the ground state and Rydberg states, but higher-coherence laser sources are required to achieve stimulated Raman adiabatic passage and for applications to molecules. *Published by AIP Publishing.* https://doi.org/10.1063/1.4997624

I. INTRODUCTION

Rydberg states of molecules are a relatively unexplored area of molecular physics. High resolution spectra of molecular Rydberg states will enable precision measurements of the properties of molecular cations,[1–6] highly efficient Stark slowing and trapping of neutral molecules,[7–11] and identification of the physical mechanisms of electron-ion energy transfer and reaction pathways in simple systems.[12–22] However, for nearly all molecules, the ionization threshold lies at a much higher energy than the dissociation threshold. As a result, long-lived Rydberg states can generally only be populated via sequential excitation steps through electronic states that are profoundly affected by rapid predissociation. The predissociation rate in Rydberg states scales as the square of the overlap of the Rydberg electron wavefunction with the ion-core; thus the rate scales as n^{*-3} and roughly as ℓ^{-7}, where n^* is the effective principal quantum number ($n^* = n - \delta_\ell$, where n is the principal quantum number and δ_ℓ is the ℓ-dependent quantum defect) and ℓ is the orbital angular momentum.[16]

Rydberg states of molecules can be divided into two categories: core-penetrating (CP) and core-nonpenetrating (CNP). CP states are those in which the wavefunction of the Rydberg electron has significant amplitude within the ion-core because it possesses relatively low orbital angular momentum. However, owing to multipolar mixing that is especially strong when the Rydberg electron is near the ion-core, ℓ is typically not a good quantum number in molecules. CP states are easily accessed from low-lying electronic states (usually the electronic ground state) because of optical transition propensity rules. CNP states are those with a relatively large orbital angular momentum ($\ell \geq 4$, in general) and small quantum defects ($\delta_\ell < 0.05$) and have received considerably less attention than the CP states, largely due to the difficulty in accessing them via optical transitions from low-lying valence states. Owing to the $\ell(\ell+1)/2r^2$ centrifugal barrier in the effective radial potential of the Rydberg electron, the wavefunction of the Rydberg electron in a CNP state has negligible amplitude within the ion-core. Predissociation lifetimes of CNP states are generally on the order of 10^{-7} to 10^{-4} s, compared with 10^{-11} to 10^{-9} s for CP states.[23,24]

Standard incoherent multiple resonance techniques, by which population is transferred one step at a time, are generally incapable of transferring a spectroscopically useful population into a CNP state by transit through a CP state with a sub-nanosecond lifetime. Coherent population transfer methods, such as STIRAP (STImulated Raman Adiabatic Passage), on the other hand, are well suited for the efficient transfer of population to CNP states because they do not suffer from the large decay rates associated with the easily accessible CP states. STIRAP has been demonstrated in a variety of systems to be capable of robust transfer of 100% of population through a short lifetime state or even significant transfer through a continuum.[25–31] However, before STIRAP can be attempted, coherence must be established between the optical photon that excites a CP state and a significantly lower frequency photon [a millimeter-wave (mm-wave) photon in our case] that excites a transition from the CP state to a CNP state. These two photons have frequencies different by more than 3 orders of magnitude. This frequency ratio is a source of difficulty in satisfying the requirements for coherent population transfer.

We report here on a demonstration of coherent, optical-mm-wave, two-photon population transfer to Rydberg states of barium as a proof-of-principle for future applications of coherent population transfer. Our choice of mm-waves was motivated by (i) the easily available long coherence times from solid-state mm-wave generation systems, (ii) the large

a)Current address: Sandia National Laboratories, Albuquerque, New Mexico 87185, USA.
b)Electronic mail: rwfield@mit.edu

transition dipole moments (on the order of 1000 D at $n^* \approx 30$) for electronic Rydberg–Rydberg transitions with small Δn^*, and (iii) the ability to simultaneously and distinctly monitor multiple transitions by detecting the Free Induction Decay (FID) associated with each transition directly in the time domain.[32–36] The last of these motivations is perhaps the most important for being able to demonstrate coherent population transfer effects, as it allows simultaneous monitoring of not just the relative populations of the intermediate and final states but also the coherence between these intermediate and final states in the form of FID radiation. Additionally, the coherence properties of the mm-waves and large transition dipole moments associated with transitions between Rydberg states allow for coherent population transfer, albeit not true STIRAP, despite the optical photon being generated in a standard pulsed dye laser (with a pulse duration of ~7 ns and a spectral bandwidth of ~1 GHz). Once it is routinely possible to efficiently and selectively populate CNP states, it will become possible to use chirped pulse mm-wave spectroscopy to systematically interrogate molecular CNP states at high resolution, large dynamic range, and near perfect completeness.

In this paper, the experimentally achieved populations and mm-wave coherences are compared with numerical solutions of the Liouville-von Neumann equation for the time evolution of the density matrix. These calculations determine the coherent character of a pulse sequence, specify the optimal experimental parameters, and predict the efficiency of coherent population transfer, even in the presence of short lifetimes of the intermediate state. Additionally, these calculations make explicit the experimental design refinements necessary for the application of STIRAP to molecules with short-lived intermediate states.

II. EXPERIMENTAL METHODS

The energy level diagram in Fig. 1 displays the excitation scheme and relevant probe transitions. A two-photon process transfers ground state Ba $6s^2\ ^1S_0$ atoms to the $6s41d\ ^1D_2$ final state via the intermediate $6s45p\ ^1P_1$ state. Population in this intermediate state is monitored by an FID signal associated with a mm-wave transition to the $6s47d\ ^1D_2$ state, while population in the final state is monitored by an FID signal associated with a mm-wave transition to the $6s41f\ ^1F_3$ state. The pump[37] transition to the $6s45p\ ^1P_1$ state is driven by a 238.269 nm, 7.5 ns etalon-narrowed dye laser pulse. The etalon-narrowed dye laser (Lambda Physik Scanmate 2E) is pumped by an injection-seeded Nd:YAG laser, and the 476.538 nm dye laser output is frequency doubled to 238.269 nm in a β-barium borate (β-BBO) crystal.

The time-averaged bandwidth of the fundamental output of this laser was measured to be 0.02 cm^{-1} (600 MHz); however, this bandwidth takes the form of three accessible longitudinal cavity modes, each with a bandwidth of ≤250 MHz spaced by 500 MHz.[38] *Each* of these modes is significantly broader than the Fourier transform limited bandwidth of 59 MHz Full Width Half Maximum (FWHM) for a 7.5 ns (FWHM) Gaussian pulse. When carefully aligned, only one longitudinal mode is dominant, both during each pulse as

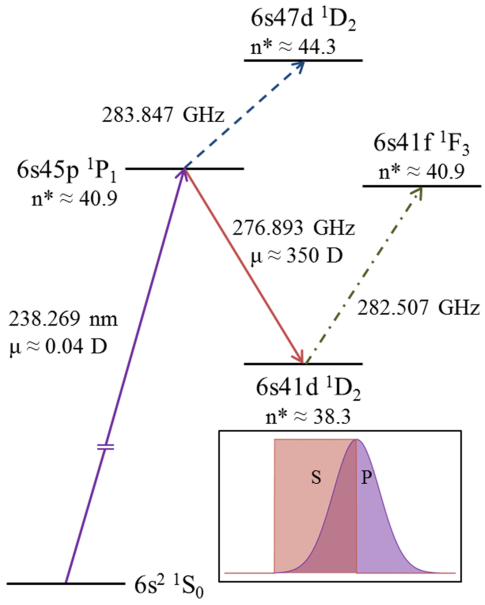

FIG. 1. Level diagram for the present experiments on the Ba atom. The pump (purple, solid), Stokes (red, solid), and probe (blue, dashed and green, dashed-dotted) transitions are shown along with the effective principal quantum numbers of each state and the electric dipole transition moments for the pump and Stokes transitions. The inset displays a cartoon that demonstrates the relative timing of the Stokes and Pump pulses required for STIRAP.

well as over the time scale of the experiment (~2 h), consistent with other lasers based on the same design.[38] The laser produced 400 μJ/pulse at the spectroscopy chamber, schematically shown in Fig. 2. This is the largest UV pulse energy that we could sustain and control over the duration of the experiment.

Millimeter-waves in the region of 260–295 GHz are required for the Stokes transition ($^1D_2 \leftarrow {}^1P_1$) and for both of the two probe transitions, and they are generated as follows. A 12.0 GS/s arbitrary waveform generator (AWG, Agilent M8150) creates pulses with frequency components from 2.0 to 3.5 GHz. These pulses are then mixed with the output of an 8.8 GHz phase-locked oscillator, filtered to select the upper sideband (10.8–13.3 GHz), and inputted to an active multiplier chain (AMC, Virginia Diodes AMC291) in which the frequency is multiplied by 24. The resultant mm-wave radiation is broadcast through a 24-dBi[39] standard gain horn and collimated by a 25-cm focal length, gold, off-axis parabolic mirror before interacting with the sample. Laser light is focused through a small hole in this parabolic mirror and expands while propagating collinearly with the mm-wave radiation. Both the residual mm-wave excitation radiation and the resultant mm-wave FID radiation are focused by a 10-cm focal length Teflon lens into a second identical standard gain horn. A second channel of the AWG creates a tunable local oscillator frequency in the 2.0–3.5 GHz region, which is also mixed with the output of the same 8.8 GHz phase-locked oscillator, filtered to select the upper sideband, and fed into a separate ×12 AMC (Virginia Diodes MixAMC156) before being used for the heterodyne detection of both the input radiation and the FID signal radiation through a subharmonic mixer. The low frequency output of this mixing process is directly detected on a 50 GS/s, 20 GHz digital oscilloscope (Tektronix DPO72004).

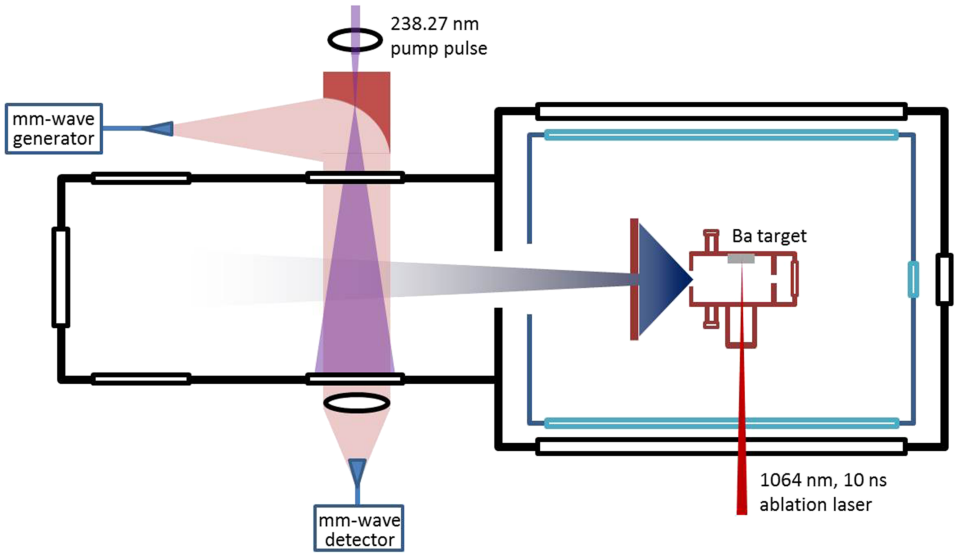

FIG. 2. Schematic diagram of the experimental setup. The important feature of the setup is that the atomic beam propagates perpendicularly to the parallel propagating pump and Stokes radiation.

The oscilloscope, AWG, and 8.8 GHz fixed frequency oscillator are all locked to the output of a 10 MHz rubidium frequency standard (Stanford Research Systems FS725) in order to phase-coherently average the time domain signal. All results discussed in this paper have been averaged over 1000 laser shots. The mm-wave system produces 30 mW of power, which we use unattenuated in order to drive the Stokes transition as strongly as possible with a 10 ns duration pulse centered at 276.893 GHz.

Due to the large electric dipole transition moments for transitions between Rydberg states, the probe transitions are very easily power broadened. The probe pulse used to monitor population in the $6s41d\ ^1D_2$ final state is attenuated by reducing the input power from the AWG to the AMC. Due to the highly nonlinear response of the AMC, changes in the input power by less than 1% can induce significant changes in the output power, making it difficult to optimize the intensity of this probe pulse by attenuation of the AWG alone. We used the duration of the probe pulse as an additional variable to adjust the degree of polarization of this probe transition. The probe transition used to monitor the $6s45p\ ^1P_1$ intermediate state was sufficiently weak that no attenuation was used. The two probe pulses consisted of one strongly attenuated 50 ns single-frequency pulse centered at 282.507 GHz (final state probe) followed immediately by an unattenuated 250 ns single-frequency pulse centered at 283.847 GHz (intermediate state probe). The first pulse induced a polarization modulo-2π of $\pi/2$ while the second pulse induced one of $\pi/4$. A polarization of modulo-2π of $\pi/2$ for the first probe was chosen to maximize the FID intensity, while the polarization of $\pi/4$ for the second pulse was chosen as a balance between FID signal intensity and competing dephasing processes. The ratio of these polarizations is used to normalize each of the probe transition intensities and determine accurate relative populations. In addition to the FID from the two probe transitions, the FID from the Stokes transition can also be detected as an additional probe of the system.

Barium atoms are excited in a buffer gas cooled atomic beam, formed similar to that in Ref. 2, summarized here.[2,40–43] Barium atoms are generated by ablation of a barium target with a ≤50 mJ pulse of the 1064 nm fundamental of a Nd:YAG laser, focused to a ~1 mm^2 spot size. We allow the Q-switch to remain open after the initial laser pulse, which causes post-ablation localized melting of the Ba target. This results in an increase of the usable lifetime of the Ba pellet to over 10 h from less than 1 h. A cold, collimated beam of Ba atoms is formed by entraining the ablation plume in a constant, 20 SCCM (standard cubic centimeters per minute) flow of 20 K neon, and a hydrodynamic expansion into vacuum through a 2 cm diameter skimmer, which is held at 6 K. The laser and mm-wave pulses intersect this atomic beam transversely 30 cm downstream from the formation area in a separate detection chamber. The choice of Ba as the target atom was motivated by (i) the low ionization potential of barium, which allows for excitation to Rydberg states with a single dye laser photon, and (ii) the ease of creating barium in the gas phase via ablation in our buffer gas cooled beam chamber (compared with, e.g., alkali metals).

In order to operate at Ba atomic number densities sufficiently low to avoid dipole-dipole interactions yet maintain a sufficient number of polarized Ba atom FID-emitters to permit the detection of FID, the resonance region is located far downstream from the skimmer in order to produce a large active experimental volume. The active volume is determined by the overlap of the laser and mm-wave radiation and the atomic beam. The mm-wave radiation determines two dimensions of the overlap region, as it is collimated to a ~1.5 cm beam diameter through the detection chamber. The divergence of the atomic beam is calculated using the relationship given in the work of Hutzler *et al.*,[42]

$$\Delta\theta \approx \sqrt{\frac{m_b}{m_s}} = 43.6^\circ, \tag{1}$$

where $\Delta\theta$ is the angular divergence, m_b is the mass of the buffer gas (neon), and m_s is the mass of the entrained species (barium). Using the diameter of the cold skimmer plate as a reference point, we calculate that the atomic beam has diverged to a ~15 cm diameter in the detection region. Combining this with

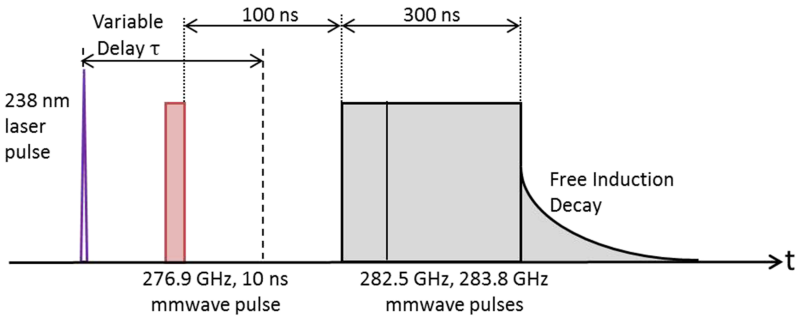

FIG. 3. The timing sequence for the laser, mm-waves, and FID. The first, purple pulse is the pump pulse, which is stepped through a variable delay τ with respect to the second, red, Stokes pulse. The two probe pulses occur 100 ns after the Stokes pulse. The double-headed arrow associated with the variable delay shows a range of delays, while the actual delay shown is for a negative value of τ.

the ~1.5 cm beam diameter of the mm-waves, we determine an active volume of $1.5\times1.5\times15 \approx 30$ cm^3. In order to match the beam diameter of the laser to that of the mm-waves, the focal properties of the laser beam were chosen such that it enters the chamber at a ~1.5 cm beam diameter and expands in area by a factor of 2 as it traverses the active volume. This expansion of the laser beam means that the Rabi frequency induced by the laser decreases over the length of the sample, resulting in a reduction in the coherent population transfer efficiency as a function of the transverse location. We observe that recollimation of the laser results in unacceptable diffractive losses of the mm-waves by the collimation optics.

A diagram of the timing of the various radiation pulses is shown in Fig. 3. In order to maintain phase coherence between all components of the experiment, the master delay generator (Stanford Research Systems Model DG535) for the experiment was locked to the same 10 MHz reference as the oscilloscope and mm-wave generation components. The leading edge of the Stokes mm-wave pulse occurs 100 ns in advance of the two probe pulses. This delay between Stokes and probe pulses allows sufficient time for damping of reflections inside the vacuum chamber. The dephasing rates of the intermediate and final states are Doppler limited at 5 μs, so this 100 ns delay does not strongly affect the signal strength. Population decay due to spontaneous decay or blackbody induced decay take place on much longer time scales (~20 ms and ~50 μs, respectively) and similarly do not strongly affect the signal strength. The leading edge of the Pump laser pulse is stepped in 500 ps increments through the leading edge of the Stokes pulse in order to observe the dependence of the transfer efficiency on the Stokes/Pump time delay.

III. THEORETICAL BACKGROUND

In order to predict the required intensities for the pump and Stokes pulses, the appropriate timing for optimal transfer, and to compare experimental results to expected signal strengths, we numerically simulate the radiation-coupled three-level system. The basic three-level Hamiltonian is given in the interaction picture by

$$H_I(t) = \frac{\hbar}{2}\begin{bmatrix} 0 & \Omega_P(t) & 0 \\ \Omega_P(t) & 2\Delta_P - i/T_1 & \Omega_S(t) \\ 0 & \Omega_S(t) & 2(\Delta_P - \Delta_S) \end{bmatrix}, \quad (2)$$

where Ω_P and Ω_S are the Rabi frequencies of the pump and Stokes pulses, Δ_P and Δ_S are the detunings of the pump and Stokes pulses from resonance, and T_1 is the incoherent decay lifetime from the intermediate state. $(\Delta_P - \Delta_S) = 0$ is chosen throughout this paper, satisfying the two-photon resonance condition. $\Omega_{P/S}$ are given by

$$\Omega_{P/S} = \frac{\mu_{P/S}\mathcal{E}_{P/S}(t)}{\hbar}, \quad (3)$$

where μ_P and μ_S are the electric dipole transition moments of the pump and Stokes transitions and $\mathcal{E}_P(t)$ and $\mathcal{E}_S(t)$ are the envelopes of the electric fields of the Pump and Stokes pulses. For the majority of calculations below, the term that includes T_1 was set to 0 to simulate an atomic system, as the primary sources of decay in atomic Rydberg systems, spontaneous and black-body induced decay, occur on much longer time scales than the STIRAP pulses, and we operate below the first ionization threshold of Ba, removing the possibility of autoionization. As opposed to a numerical solution of the time-dependent Schrödinger equation, as is commonly used to simulate STIRAP, we solved the Liouville-von Neumann equation in order to calculate the coherences between atomic states

$$i\hbar\frac{\partial\rho}{\partial t} = [H_I, \rho], \quad (4)$$

where ρ is the density matrix. For an n-level system, the density matrix is an n × n matrix where the diagonal terms represent the populations of the individual levels and the off-diagonal terms represent the coherences between connected levels. Applying Eq. (4) to the Hamiltonian in Eq. (2) results in the following system of nine coupled differential equations:

$$i\dot{\rho}_{11} = \Omega_P(\rho_{21} - \rho_{12}), \quad (5a)$$

$$i\dot{\rho}_{12} = \Omega_P\rho_{22} - \Omega_P^*\rho_{11} - \Omega_S\rho_{13} - \left(2\Delta_P + \frac{i}{T_1}\right)\rho_{12}, \quad (5b)$$

$$i\dot{\rho}_{13} = \Omega_P\rho_{23} - \Omega_S\rho_{12} - 2(\Delta_P - \Delta_S)\rho_{13}, \quad (5c)$$

$$i\dot{\rho}_{21} = \Omega_P^*\rho_{11} - \Omega_P\rho_{22} + \Omega_S\rho_{31} + \left(2\Delta_P - \frac{i}{T_1}\right)\rho_{21}, \quad (5d)$$

$$i\dot{\rho}_{22} = \Omega_P^*(\rho_{12} - \rho_{21}) + \Omega_S(\rho_{32} - \rho_{23}) - \frac{2i}{T_1}\rho_{22}, \quad (5e)$$

$$i\dot{\rho}_{23} = \Omega_P^*\rho_{13} - \Omega_S(\rho_{33} - \rho_{22}) + \left(2\Delta_S - \frac{i}{T_1}\right)\rho_{23}, \quad (5f)$$

$$i\dot{\rho}_{31} = -\Omega_P\rho_{32} + \Omega_S\rho_{21} + 2(\Delta_P - \Delta_S)\rho_{31}, \quad (5g)$$

$$i\dot{\rho}_{32} = -\Omega_P^*\rho_{31} - \Omega_S(\rho_{22} - \rho_{33}) - \left(2\Delta_S + \frac{i}{T_1}\right)\rho_{32}, \quad (5h)$$

$$i\dot{\rho}_{33} = \Omega_S(\rho_{23} - \rho_{32}), \quad (5i)$$

where ρ_{ij} are the density matrix elements and Ω_P^* is the complex conjugate of the complex pump Rabi frequency given below. This complex Rabi frequency is introduced to account for the possibility of phase noise in the pump laser beam. The off-diagonal terms are related to the amplitude of the FID radiation by

$$\mathrm{FID}_{ij} \propto |i(\rho_{ij} - \rho_{ji})|, \tag{6}$$

where $i \neq j$. In many applications of STIRAP, in which the intermediate state is very short-lived, the coherences that involve the intermediate state decay at a rate comparable to that of the population in the intermediate state. Thus the coherences that involve the intermediate state are typically difficult to observe. However, for our proof-of-principle experiments, the intermediate state is long-lived, and the coherence that builds up between the intermediate and final states is directly detectable as FID. This coherence provides a parameter in addition to population transfer that will indicate whether the STIRAP process is occurring.

The characteristic effect in the coherence [as in Eq. (6)] that demonstrates the occurrence of STIRAP is a decrease to zero of the coherence between the intermediate and final states when the pump pulse arrives slightly later than the Stokes pulse, in the so-called "counter-intuitive" pulse sequence. This implies that there is no transient population in the intermediate state. This decrease in coherence can be seen clearly as the pump Rabi frequency is increased, shown in Fig. 4. Figures 4(d)–4(f) display the coherence between the intermediate and final states as a function of the relative timing of the pump and Stokes pulses, τ. For negative values of τ, the center of the pump pulse occurs before the center of the Stokes pulse, which is the so-called "intuitive" pulse sequence, as shown in Fig. 4(a) and indicated by the vertical red dashed lines in Figs. 4(d)–4(f). For positive values of τ, the center of the pump pulse occurs after the center of the Stokes pulse, as shown in Fig. 4(c) and indicated by the vertical black dashed-dotted lines in Figs. 4(d)–4(f). The "counter-intuitive" pulse sequence is shown in Fig. 4(b) and corresponds to the ideal overlap between the Stokes and pump pulses, $\tau \sim 5$ ns. This value of τ corresponds to the Stokes pulse arriving first and is indicated by the vertical green solid lines in Figs. 4(d)–4(f). The rapid oscillations shown in Fig. 4(d) are two-photon Rabi oscillations that occur as the pump and Stokes pulses move through a complete overlap. The coherence between the intermediate and final states has a pronounced minimum at the counter-intuitive pulse sequence in plot (d), as expected for STIRAP. The final state populations for each of these cases are shown in Fig. 5. Two-photon Rabi oscillations are pronounced in the population as a function of the pulse overlap as well.

In order to account for the poor phase coherence properties and large intensity fluctuations of the pulsed dye laser pump pulse, we include these fluctuations directly in our calculations and average the simulation results in an attempt to replicate the experimental results. For the phase fluctuations, we include

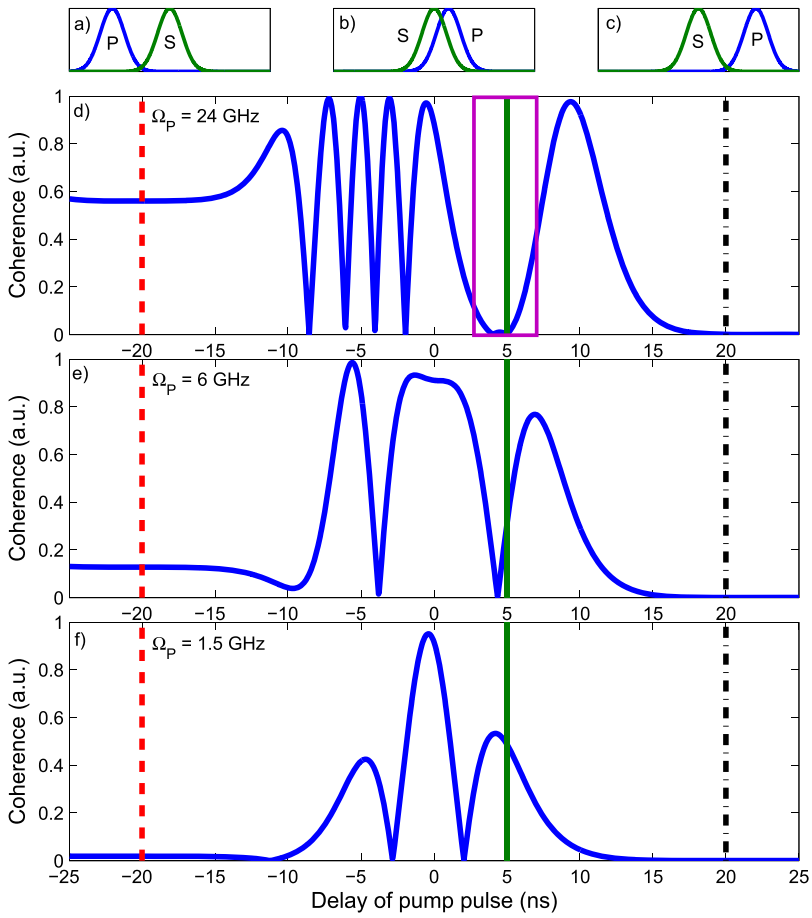

FIG. 4. Dependence on the pump Rabi frequency and on the pump-Stokes delay of the coherence between the intermediate and final states. Plots (a)–(c) display the pulse timings at negative, small positive, and large positive values of the pump pulse delay. Plots (d)–(f) display the coherence for a pair of 10 ns pulses with 24 GHz, 6 GHz, and 1.5 GHz Pump Rabi frequencies, respectively. The vertical dashed, solid, and dashed-dotted lines indicate the relative pump and Stokes pulse timings displayed in plots (a)–(c). The purple boxed area in plot (d) displays the minimum in the coherence associated with STIRAP.

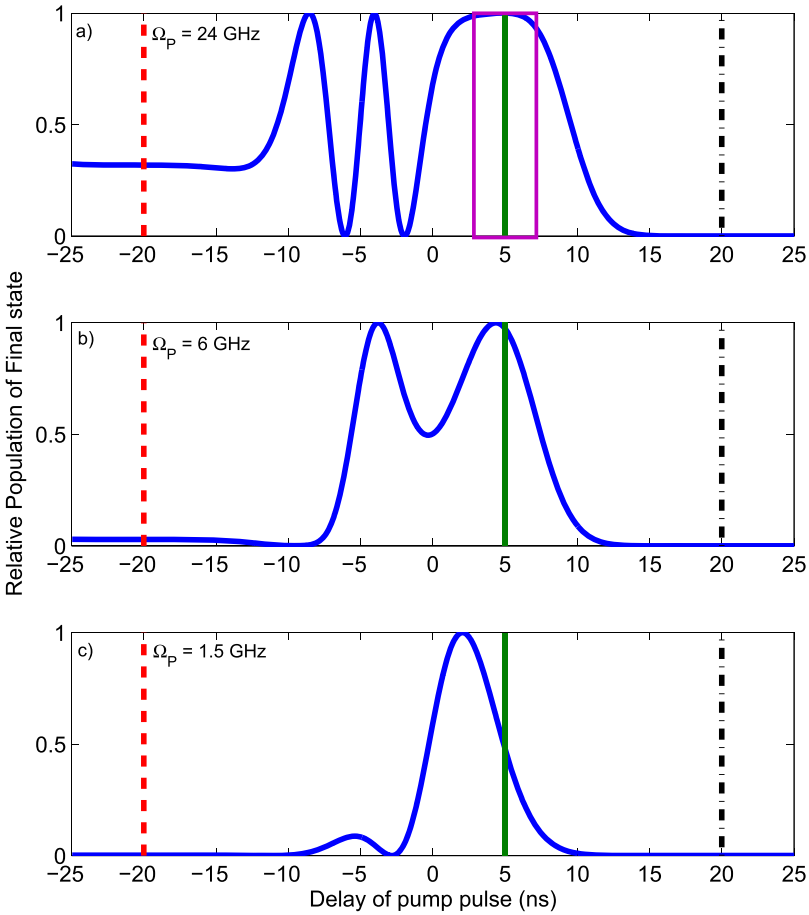

FIG. 5. Dependence on the pump Rabi frequency and on the Pump-Stokes delay of the final state population. Plots (a)–(c) display the final state population for a pair of 10 ns pulses with 24 GHz, 6 GHz, and 1.5 GHz Pump Rabi frequencies, respectively. The vertical dashed, solid, and dashed-dotted lines indicate the relative pump and Stokes pulse timings as in Fig. 4. The purple boxed area in plot (a) displays the full population transfer associated with STIRAP.

exponentially correlated colored phase noise, equivalent to a phase diffusion model with a non-Lorentzian line shape.[27] This takes the form of a pseudo-random phase function, $\alpha(t)$, which modulates the pump pulse, leading to a modification of the Rabi frequency,

$$\Omega_P = \frac{\mu_P \mathcal{E}_P(t) e^{i\alpha(t)}}{\hbar}. \tag{7}$$

The phase function $\alpha(t)$ depends on two parameters, the spectral density of the noise, D, and the correlation time of the fluctuations, Γ, given by the correlation function

$$\langle \epsilon(t)\epsilon(s)\rangle = D\Gamma e^{-\Gamma|t-s|}, \tag{8}$$

where t and s are two arbitrary times. $\alpha(t)$ can then be generated using the Box-Müller algorithm.[27] D and Γ also describe the ratio of the laser bandwidth to that of the Fourier transform limited pulse, $N_{Fourier}$, by the relationship

$$N_{Fourier} = \frac{\Delta\omega_{Phase}}{\Delta\omega_{Fourier}} = \Delta t_{Laser}\sqrt{\frac{D\Gamma}{2}}, \tag{9}$$

where Δt_{Laser} is the FWHM of the duration of the laser pulse, $\Delta\omega_{Phase}$ is the FWHM of the frequency of the simulated laser pulse, and $\Delta\omega_{Fourier}$ is the FWHM of the frequency of a Fourier transform limited pulse of duration Δt_{Laser}. In order to simulate a non-transform limited pulse that matches a single longitudinal mode of our intracavity etalon-narrowed pulsed dye laser ($\Delta\omega_{Phase} \approx 250$ MHz, $N_{Fourier} \approx 4$), we set $D = \Gamma = 0.75$ GHz. Different values of D and Γ that maintained a constant value of $\sqrt{D\Gamma/2}$ were investigated, with qualitatively similar results for small variations in D and Γ, which match the conclusions of Ref. 27.

Intensity fluctuations were included by modifying the electric field, and hence the Rabi frequency, of the pump laser pulse. The nominal pump laser field was multiplied by a pseudo-random number chosen from a Gaussian distribution with a fractional variance of 0.075, chosen to match the intensity fluctuations observed for our laser. The temporal profile of the dye laser pulse is measured to be nearly Gaussian with a 7.5 ns FWHM.

The mm-wave source has vastly better coherence properties and fewer intensity fluctuations than the pulsed dye laser. The primary limitation of our mm-wave source is that the pulse-generating electronics have response times on the order of several nanoseconds and cannot easily produce outputs with amplitude shaping on time scales shorter than a few ns. The Stokes pulse, therefore, takes the form of a 10 ns Fourier-transform limited (Fourier transform limit FWHM of ~120 MHz) square wave pulse exactly centered on resonance with the Ba Rydberg–Rydberg transition. Non-adiabatic losses from the sudden turn-off of the Stokes pulse are unavoidable with a square wave pulse, and we have also simulated the pulse with a Gaussian and a triangular pulse shape in an attempt to quantify these losses.

IV. RESULTS AND ANALYSIS

The solid curves in Fig. 6(a) show the ratio of transition intensity of the $41f - 41d$ transition (probe of final level) to

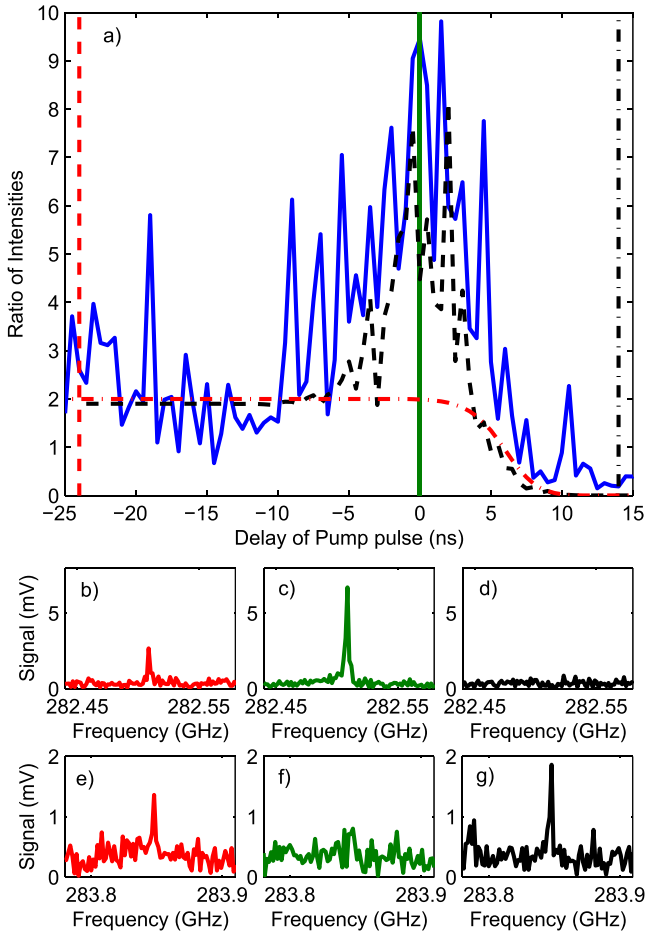

FIG. 6. Plot (a) displays the experimental ratio of the population in the final state to the population in the intermediate state as a function of the pump pulse delay, τ, as a blue solid curve, the coherent theoretical results as a black dashed curve, and the incoherent theoretical results as a red dashed-dotted curve. The vertical axis of plot (a) is the ratio of FID intensities, which is related to the ratio of populations by the ratio of the pulse areas of the two-probe pulses. Plots (b)–(d) display the intensity of the $41f - 41d$ transition (probe of the final level) at pump pulse delays given by the vertical red dashed line, the vertical green solid line, and the vertical black dashed-dotted line in plot (a), respectively. Plots (e)–(g) display the intensity of the $47d - 45p$ (probe of the intermediate level) transition at the same pulse delays. Note the difference in vertical scales between plots (b)–(d) and plots (e)–(g).

the transition intensity of the $47d - 45p$ transition (probe of intermediate level), weighted by the difference in probe pulse excitation areas ($\pi/2$ for the $41f - 41d$ transition and $\pi/4$ for the $47d - 45p$ transition), as a function of the variable delay, τ, of the laser pump pulse. The observation of a maximum at a delay $\tau = 0$, the time at which the center of the laser (pump) pulse is coincident with the center of the mm-wave (Stokes) pulse, demonstrates enhanced transfer when *both* radiation fields are present *at the same time*. As in Fig. 4, for negative values of τ, the center of the pump pulse occurs before the center of the Stokes pulse while positive values of τ correspond to the center of the pump pulse occurring after the center of the Stokes pulse. For negative values of τ, the ratio of transition intensities is dictated primarily by the efficiencies of the pump and Stokes pulses in transferring population via separate one-photon processes, while for large positive values of τ, no population is expected to be transferred to the final state. All coherent transfer processes are expected to occur when τ is small and positive or when $\tau \approx 0$.

Figures 6(b)–6(d) show the intensity of the $41d - 41f$, final state probe transition, and Figs. 6(e)–6(g) show the intensity of the $45p - 47d$, intermediate state probe transition at the delays indicated by the vertical dashed, solid, and dashed-dotted lines, respectively. At a delay consistent with the intuitive pulse sequence [Figs. 5(b) and 5(e)], both the intermediate and final states retain population, thus probe transitions from both states are observed. As the pulses begin to overlap [Figs. 5(c) and 5(f)], the intensity in the probe transition that originates from the final state increases significantly, while the probe transition out of the intermediate state disappears entirely. Finally, when the pump pulse is delayed to occur entirely after the Stokes pulse such that there is no overlap between the two pulses, the probe transition out of the final state disappears [Figs. 5(d) and 5(g)], while the probe transition out of the intermediate state increases significantly in intensity. Note that this does not correspond to the counter-intuitive pulse sequence, and we observe no enhancement at timing consistent with the counter-intuitive pulse sequence.

The dashed black curve in Fig. 6(a) shows the results of our calculations of coherent effects, which include phase and intensity noise effects, as outlined above, while the dashed-dotted red curve in Fig. 6(a) shows the results of a calculation of an incoherent transition sequence using Einstein rate coefficients, displayed as the ratio of the intensity of the probe transition associated with the final state to the probe transition associated with the intermediate state. This ratio is related to the ratio of populations by the ratio of the pulse areas of the two probe pulses. Qualitatively, the dependence on τ of the experimental data is well reproduced in the coherent calculations, in contrast to the qualitative disagreement between the experimental observations and the incoherent calculations.

This agreement of the coherent calculations for the ratio of final to intermediate populations supports the validity of our calculations of the population transferred into the final state when the pulses are overlapped and we expect to find good agreement with our experimental results. The model system shows a population transfer from the initial state to the final state of ~50% during exact overlap, compared with a transfer of ~20% for both the intuitive ($\tau \lesssim -5$ ns) and counter-intuitive ($\tau \approx 5$ ns) pulse sequences. The calculated variation of the final state population with a delay time of the pump pulse is shown in the solid blue curve of Fig. 7(a).

The primary factor that limits the efficiency of the two-photon process is the phase fluctuations associated with the pump pulse generated by our pulsed dye laser. Previous theoretical and experimental studies of the use of pulsed dye lasers in coherent population transfer techniques, such as STIRAP, have shown that the Rabi frequency required to drive these processes scales as $N_{Fourier}^2$ [see Eq. (9)].[25,27,29] In our system, $N_{Fourier} \approx 4$ for each longitudinal mode, leading to an ~16× effective reduction in the Rabi frequency for the pump pulse. The absence of an improvement in population transfer for the counter-intuitive pulse sequence as compared with what we observe for completely overlapped pulses, as well as a

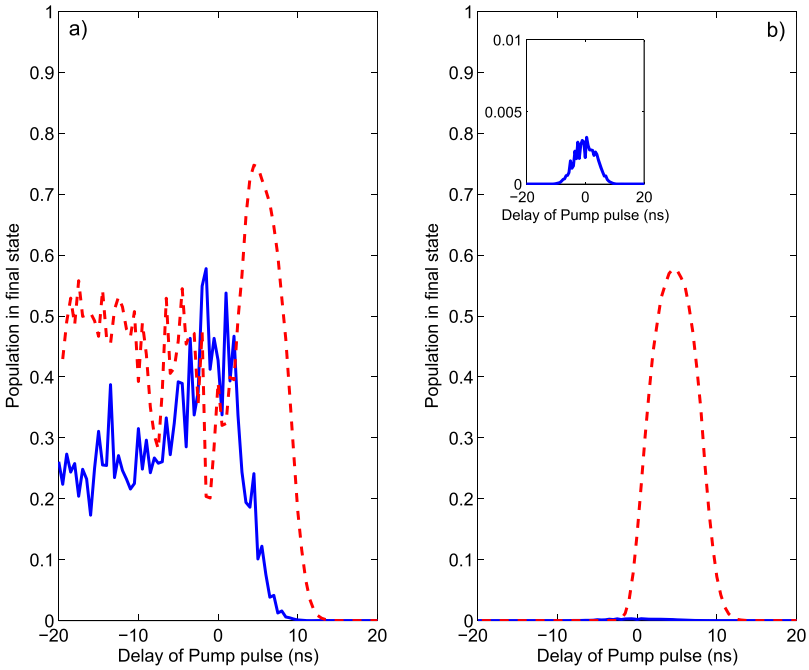

FIG. 7. Theoretical populations of the final state as a function of the pump pulse delay, τ, without (a) and with (b) intermediate state decay due to predissociation. Solid curves indicate conditions that match our experimental conditions; dashed curves indicate simulations for calcium as outlined in the text. The inset to plot (b) is a zoom in of the very low population transfer shown by the solid curve.

maximum population transfer efficiency of only ~50% imply that STIRAP is *not occurring* for the laser conditions presently obtained in our system. With the limited power available from our dye laser in the UV, we cannot reach the regime of STIRAP because the effective Rabi frequency for the first transition is too low. This conclusion is experimentally supported by our observation of the remaining coherence between the intermediate and final states, which is manifest as FID radiation at the frequency of the Stokes pulse. The solid curve in Fig. 8(a) shows the FID associated with the $45p - 41d$ transition as a function of the delay of the laser pump pulse, while the dashed curve shows the calculated coherence [as in Eq. (6)] between the two states. The decrease in coherence near small, positive Stokes-pump delays characteristic of the STIRAP process is also absent in both of these curves. The observed increase in the population transfer efficiency when the pulses are overlapped is still, however, evidence of coherent population transfer, in a more straightforward two-photon Raman scheme where the population of the intermediate state is transient, as opposed to a STIRAP scheme where the population of the intermediate state remains zero.

In order to determine whether optical-mm-wave STIRAP is feasible using a pulsed dye laser similar to the one available for our experiments, we simulate a realistic target system based on known transitions in atomic calcium. With a larger ionization potential, we can use a two-step optical excitation

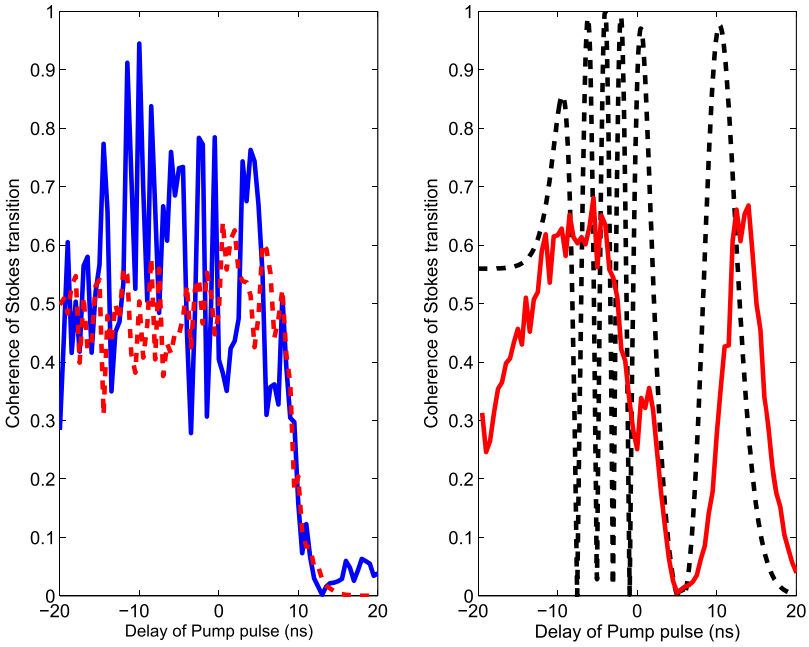

FIG. 8. Coherence between the intermediate and final states [as in Eq. (6)] as a function of the variable delay of the pump pulse. Plot (a) displays the experimental (blue solid) and calculated (red dashed) coherences for our actual experimental conditions. Plot (b) displays the calculated (red solid) coherence for calcium simulations as described in the text and the coherence expected for a system with two Gaussian pulses as described in Sec. III and displayed in Fig. 4(d) (black dashed-dotted).

path to Rydberg states ($4snd \leftarrow 4s5p \leftarrow 4s^2$, corresponding to transition wavelengths of ~272 nm and ~803 nm) in order to exploit a larger pump electric dipole transition moment of ~0.5 D, and take advantage of the higher available pump laser power in the IR of ~ 2 mJ. Ca, in particular, is a useful atom due to the similarity between the structure of the Rydberg states of Ca and those of CaF, a prototypical molecular target.[44]

When calculating the population transferred to the final state with this realistic system, we observe a maximum associated with STIRAP that occurs at the optimum Stokes-pump delay of the counter-intuitive pulse sequence, as shown in the dashed curve of Fig. 7(a). Additionally, we observe the characteristic decrease to zero in the coherence between the intermediate and final states at the same pulse timing as displayed by the dashed curve in Fig. 8(b). The solid curve in Fig. 8(b) shows a system with two Gaussian pulses, as discussed in Sec. III [and is the same curve as in Fig. 4(d)]. These distinct decreases in coherence between the intermediate and final states at $\tau \sim 5$ ns delay in both curves are associated with the STIRAP mechanism of transferring population directly from the initial to the final state without placing any population in the intermediate state. These two calculations demonstrate that the primary obstacle remaining to achieve optical-mm-wave STIRAP is to increase the Rabi frequency for the pump transition, either by increasing laser power, changing the excitation scheme to exploit a larger transition dipole moment, or by improving the coherence properties of the laser.

In order to more accurately predict the transfer efficiency in the case of a rapidly predissociating molecule, we set T_1 in Eq. (2) to 100 ps in order to replicate typical predissociation lifetimes in the intermediate state and recalculate with our current experimental parameters. The population of the final state as a function of the pump laser delay is shown as the solid curve in the inset to Fig. 7(b). A maximum transfer efficiency of less than 1% is predicted. In contrast, the population in the final state with a predissociated intermediate state for the calcium system, as outlined above, is displayed as the dashed curve in Fig. 7(b), which shows a maximum of ~60% population transfer.

The failure to achieve near 100% transfer of population from the initial state to the final state in this realistic system is due to other experimental imperfections in our system, such as the non-adiabatic losses inherent in the sharp turn-off of the mm-wave pulse. The transfer efficiency may be modeled as a function of the mm-wave pulse shape (square wave, Gaussian, triangle pulse), and the results are shown in Fig. 9. These calculations used a 100 ps value of T_1 and parameters from the calcium system. As expected, a Gaussian pulse provides the most efficient transfer, but a triangle pulse provides nearly the same efficiency and is technically easier to implement.

As the frequencies of the laser and mm-wave photons are different by a factor of $\sim 10^3$, the Doppler shifts of the two transitions are quite different and result in a two-photon detuning that cannot be compensated for by any choice of experimental geometry. For a Λ-type transition, co-propagating beams of *similar frequency* cancel the majority of the Doppler shift, while for a ladder-type transition, counter-propagating beams of similar frequency have the same effect. In our case, the

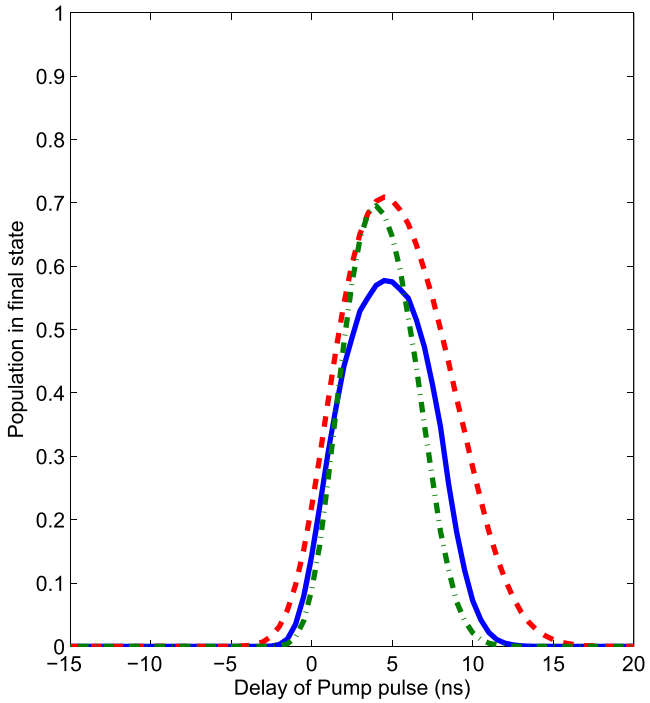

FIG. 9. Computed populations of the final state as a function of the Stokes pulse envelope. The blue solid curve represents a square pulse envelope, the red dashed curve represents a Gaussian pulse envelope, and the green dashed-dotted curve represents a triangular pulse envelope. All calculations were performed on the calcium system as described in the text.

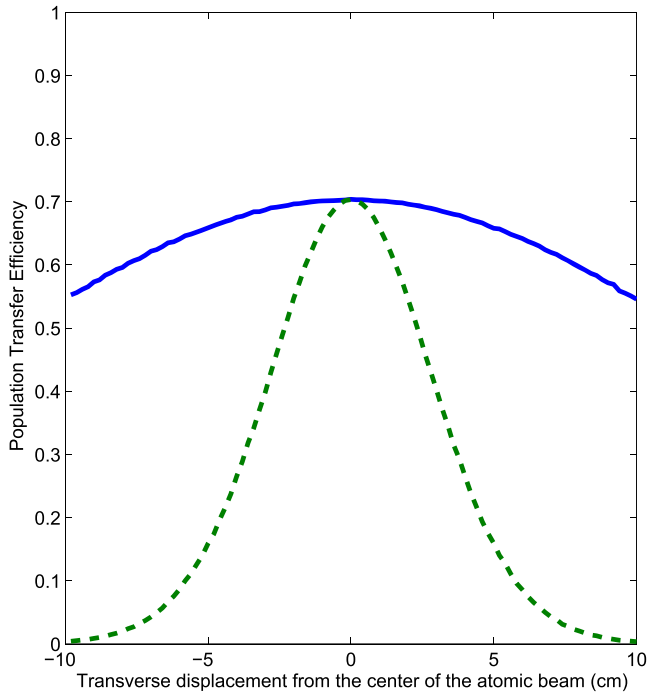

FIG. 10. Computed population transfer efficiency as a function of the transverse distance from the center of the atomic beam. The blue solid curve represents a slow buffer gas cooled expansion and the green dashed curve represents a fast supersonic expansion. All calculations were performed on the calcium system as described in the text.

Doppler width associated with the optical photon (~800 MHz) is much larger than the Doppler width associated with the mm-wave photon (~200 kHz). These small Doppler widths are due to the use of a buffer gas cooled beam source in our experiments. Typical Doppler widths in a supersonic expansion are ~5× larger. We calculate the efficiency of STIRAP transfer in Ca for both a slow buffer gas expansion and a fast supersonic expansion as a function of the radial distance from the center of the beam. The results of this calculation are shown in Fig. 10. For systems with a large frequency mismatch between pump and Stokes pulses, it is clear that a slow beam expansion, such as obtained from buffer gas cooling, is essential to achieve efficient population transfer across the entire sample.

V. CONCLUSION

We have demonstrated coherent coupling between an optical and a mm-wave photon that differ in frequency by a factor of $\sim 10^3$. This is a proof-of-principle that demonstrates the feasibility of observation and exploitation of optical-mm-wave STIRAP for the efficient coherent population transfer to CNP Rydberg states of predissociating molecules. We have performed simulations that employ a density matrix formalism to capture coherences (FID) as well as population transfer. These simulations allow an accurate calculation of the experimental parameters required to optimize this transfer, as well as to evaluate the dominant sources of non-ideality. Alkaline-earth monohalide molecules, such as CaF, will be the first molecular target for this experimental technique due to their large ion-core dipole moments, closed-shell ion-core electronic structure, and the similarity of their Rydberg states to those of the alkaline earth atoms used in these proof-of-principle experiments.

The two most important improvements for our system required to ensure maximization of the efficiency of molecular population transfer are reduction of the phase noise in the pump laser and shaping of the temporal envelope of the mm-wave pulse to minimize non-adiabatic losses. We are constructing a pulsed amplifier for a phase-stable CW laser system in order to create a pulsed laser system with the near Fourier transform limited bandwidth. The pump source for this amplifier will ideally have a pulse duration of ≥10 ns which is sufficiently long to allow for shaping of the mm-wave pulse envelope with a voltage controlled attenuator.

Multi-photon ionization is also an obstacle that must be overcome, as the pump pulse can cause multi-photon ionization of the Rydberg states in either the intermediate or the final state. Higher-coherence laser sources combat ionization through reduction of non-resonant radiation that would contribute to ionization but not to STIRAP population transfer. Longer pulse durations also combat multi-photon ionization by allowing for lower peak intensities of both pulses, further minimizing unwanted ionization processes.

The relatively poor behavior of commercial pulsed dye lasers prevents realization of full optical-mm-wave STIRAP despite the superb coherence properties of the mm-wave radiation. This precludes true STIRAP even with a perfectly coherent mm-wave source. However, once the optical coherence has been improved, the coherence of the mm-waves and the large electric dipole transition moments between Rydberg states open the door for more sophisticated coherent population transfer methods with a single optical photon and a pre-selected sequence of mm-wave pulses. As predissociation lifetimes become exponentially longer as ℓ is increased, using STIRAP to enter an ng state, for example, provides a long enough lifetime for mm-wave pulses to transfer further population. Such designer-pulse schemes will enable flexibility in selective population of CNP states that lie even higher in ℓ. Once populated, we plan to use the CNP states of molecules as a first step toward a global understanding of the entire electronic structure of a molecule, in investigations of the dynamics of intramolecular electron-nuclear energy transfer, and also as a tool for creating quantum state-selected molecular ions in selected single rotation-vibration-M_J states via vibrational autoionization and Stark slowing of Rydberg molecules.

ACKNOWLEDGMENTS

We thank Professor Edward Eyler and Professor John Muenter for valuable comments and feedback and Professor Brooks Pate for equipment. This material is based upon work supported by the National Science Foundation under Grant No. CHE-1361865. D.D.G. was supported by the Department of Defense (DoD) through the National Defense Science and Engineering Graduate Fellowship (NDSEG) Program. T.J.B. was supported by the National Science Foundation Graduate Research Fellowship under Grant No. 1122374.

[1] S. R. Lundeen, Adv. At., Mol., Opt. Phys. **52**, 161 (2005).
[2] Y. Zhou, D. D. Grimes, T. J. Barnum, D. Patterson, S. L. Coy, E. Klein, J. S. Muenter, and R. W. Field, Chem. Phys. Lett. **640**, 124 (2015).
[3] J. J. Kay, S. L. Coy, V. S. Petrović, B. M. Wong, and R. W. Field, J. Chem. Phys. **128**, 194301 (2008).
[4] P. L. Jacobson, R. A. Komara, W. G. Sturrus, and S. R. Lundeen, Phys. Rev. A **62**, 1 (2000).
[5] D. T. Biernacki, S. D. Colson, and E. E. Eyler, J. Chem. Phys. **89**, 2599 (1988).
[6] D. T. Biernacki, S. D. Colson, and E. E. Eyler, J. Chem. Phys. **88**, 2099 (1988).
[7] S. D. Hogan and F. Merkt, Phys. Rev. Lett. **100**, 043001 (2008).
[8] S. Hogan, C. Seiler, and F. Merkt, Phys. Rev. Lett. **103**, 123001 (2009).
[9] C. Seiler, S. D. Hogan, and F. Merkt, Phys. Chem. Chem. Phys. **13**, 19000 (2011).
[10] S. D. Hogan, P. Allmendinger, H. Saßmannshausen, H. Schmutz, and F. Merkt, Phys. Rev. Lett. **108**, 063008 (2012).
[11] S. D. Hogan, EPJ Tech. Instrum. **3**, 2 (2016); arXiv:1603.04432v1.
[12] E. E. Eyler, Phys. Rev. A **34**, 2881 (1986).
[13] J. Jortner and M. Bixon, J. Chem. Phys. **102**, 5636 (1995).
[14] M. J. J. Vrakking and Y. T. Lee, J. Chem. Phys. **102**, 8818 (1995).
[15] M. Bixon and J. Jortner, J. Chem. Phys. **103**, 4431 (1995).
[16] M. Bixon and J. Jortner, J. Chem. Phys. **105**, 1363 (1996).
[17] H. Park, D. J. Leahy, and R. N. Zare, Phys. Rev. Lett. **76**, 1591 (1996).
[18] H. Park and R. N. Zare, J. Chem. Phys. **106**, 2239 (1997).
[19] J. Clevenger, N. Harris, R. W. Field, and J. Li, J. Mol. Spectrosc. **193**, 412 (1999).
[20] T. P. Softley, Int. Rev. Phys. Chem. **23**, 1 (2004).
[21] J. J. Kay, S. Altunata, S. L. Coy, and R. W. Field, Mol. Phys. **105**, 1661 (2007).
[22] J. J. Kay, S. L. Coy, B. M. Wong, C. Jungen, and R. W. Field, J. Chem. Phys. **134**, 114313 (2011).
[23] A. Fujii and N. Morita, J. Chem. Phys. **98**, 4581 (1993).
[24] A. Fujii and N. Morita, J. Chem. Phys. **103**, 6029 (1995).
[25] K. Bergmann, H. Theuer, and B. W. Shore, RMP Colloq. **70**, 1003 (1998).

[26]K. Bergmann, N. V. Vitanov, and B. W. Shore, J. Chem. Phys. **142**, 170901 (2015).
[27]A. Kuhn, G. W. Coulston, G. Z. He, S. Schiemann, K. Bergmann, and W. S. Warren, J. Chem. Phys. **96**, 4215 (1992).
[28]A. Kuhn, S. Steuerwald, and K. Bergmann, Eur. Phys. J. D **1**, 57 (1998).
[29]S. Schiemann, A. Kuhn, and S. Steuerwald, Phys. Rev. Lett. **71**, 3637 (1993).
[30]N. V. Vitanov and S. Stenholm, Phys. Rev. A **56**, 1463 (1997).
[31]T. Peters, L. P. Yatsenko, and T. Halfmann, Phys. Rev. Lett. **95**, 103601 (2005).
[32]G. G. Brown, B. C. Dian, K. O. Douglass, S. M. Geyer, S. T. Shipman, and B. H. Pate, Rev. Sci. Instrum. **79**, 053103 (2008).
[33]A. P. Colombo, Y. Zhou, K. Prozument, S. L. Coy, and R. W. Field, J. Chem. Phys. **138**, 014301 (2013).
[34]B. C. Dian, G. G. Brown, K. O. Douglass, and B. H. Pate, Science **320**, 924 (2008).
[35]G. B. Park, A. H. Steeves, K. Kuyanov-Prozument, J. L. Neill, and R. W. Field, J. Chem. Phys. **135**, 024202 (2011).
[36]K. Prozument, A. P. Colombo, Y. Zhou, G. B. Park, V. S. Petrović, S. L. Coy, and R. W. Field, Phys. Rev. Lett. **107**, 143001 (2011).
[37]We use the standard STIRAP terminology of pump and Stokes transitions. The optical transition is denoted as the pump transition, and the mm-wave transition is denoted as the Stokes transition.
[38]T. T. Kajava, H. M. Lauranto, and R. R. Salomaa, Appl. Opt. **31**, 6987 (1992).
[39]Decibels of gain relative to an isotropic radiator.
[40]D. Patterson, J. Rasmussen, and J. M. Doyle, New J. Phys. **11**, 055018 (2009).
[41]S. E. Maxwell, N. Brahms, R. DeCarvalho, D. R. Glenn, J. S. Helton, S. V. Nguyen, D. Patterson, J. Petricka, D. DeMille, and J. M. Doyle, Phys. Rev. Lett. **95**, 173201 (2005).
[42]N. R. Hutzler, H. I. Lu, and J. M. Doyle, Chem. Rev. **112**, 4803 (2012).
[43]D. D. Grimes, S. L. Coy, T. J. Barnum, Y. Zhou, S. F. Yelin, and R. W. Field, Phys. Rev. A **95**, 043818 (2017).
[44]S. F. Rice, H. Martin, and R. W. Field, J. Chem. Phys. **82**, 5023 (1985).